



**HAL**  
open science

## Modeling sintering anisotropy in ceramic stereolithography of silica

Charles Manière, Gabriel Kerbart, Christelle Harnois, Sylvain Marinel

► **To cite this version:**

Charles Manière, Gabriel Kerbart, Christelle Harnois, Sylvain Marinel. Modeling sintering anisotropy in ceramic stereolithography of silica. *Acta Materialia*, 2020, 182, pp.163-171. 10.1016/j.actamat.2019.10.032 . hal-02449658

**HAL Id: hal-02449658**

**<https://normandie-univ.hal.science/hal-02449658>**

Submitted on 22 Jan 2020

**HAL** is a multi-disciplinary open access archive for the deposit and dissemination of scientific research documents, whether they are published or not. The documents may come from teaching and research institutions in France or abroad, or from public or private research centers.

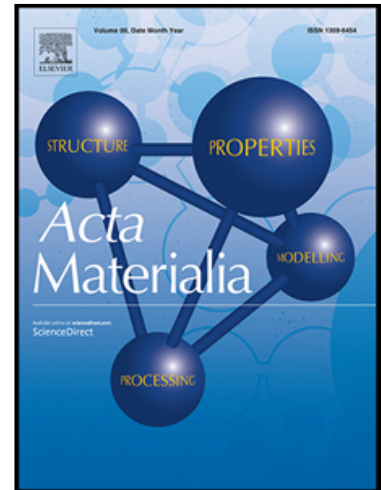
L'archive ouverte pluridisciplinaire **HAL**, est destinée au dépôt et à la diffusion de documents scientifiques de niveau recherche, publiés ou non, émanant des établissements d'enseignement et de recherche français ou étrangers, des laboratoires publics ou privés.

## Journal Pre-proof

Modeling sintering anisotropy in ceramic stereolithography of silica

Charles Manière , Gabriel Kerbart , Christelle Harnois ,  
Sylvain Marinel

PII: S1359-6454(19)30694-9  
DOI: <https://doi.org/10.1016/j.actamat.2019.10.032>  
Reference: AM 15600



To appear in: *Acta Materialia*

Received date: 29 May 2019  
Revised date: 13 September 2019  
Accepted date: 11 October 2019

Please cite this article as: Charles Manière , Gabriel Kerbart , Christelle Harnois , Sylvain Marinel , Modeling sintering anisotropy in ceramic stereolithography of silica, *Acta Materialia* (2019), doi: <https://doi.org/10.1016/j.actamat.2019.10.032>

This is a PDF file of an article that has undergone enhancements after acceptance, such as the addition of a cover page and metadata, and formatting for readability, but it is not yet the definitive version of record. This version will undergo additional copyediting, typesetting and review before it is published in its final form, but we are providing this version to give early visibility of the article. Please note that, during the production process, errors may be discovered which could affect the content, and all legal disclaimers that apply to the journal pertain.

© 2019 Published by Elsevier Ltd on behalf of Acta Materialia Inc.

**Highlights**

- Printing conditions, generation of architected porous microstructure
- Interlayer porosity microstructure implies sintering anisotropy
- Anisotropic sintering parameter identification and modeling

Journal Pre-proof

**Modeling sintering anisotropy in ceramic stereolithography of silica**Charles Manière<sup>a\*</sup>, Gabriel Kerbart<sup>a</sup>, Christelle Harnois<sup>a</sup>, Sylvain Marinel<sup>a</sup>

(a) Normandie Univ, ENSICAEN, UNICAEN, CNRS, CRISMAT, 14000, Caen, France

**Keywords**

Stereolithography; Sintering; Anisotropy; Modeling; Ceramic; Additive Manufacturing

**Abstract**

In the domain of ceramic additive manufacturing, sintering is a key step for controlling the final shape and mechanical strength of a 3D object. The thermal treatment of the printed green objects has a high influence on the specimen density, debinding, and sintered microstructure. This work focuses on the shrinkage anisotropy phenomenon that occurs during sintering. We demonstrate by dilatometry and interrupted sintering microstructure analysis that this phenomenon originates from non-ideal particle packing between the printed layers, which generates an anisotropic porosity distribution at the mesoscale. Based on this, a sintering model is developed and specially adapted for the numerical prediction of the sintering anisotropy. This model is formulated in analytic equations that can easily identify all the model parameters and reproduce the experimental dimensional changes. This numerical tool can be of great assistance in the prediction of additive manufacturing object dimensional changes during sintering.

---

\* Corresponding author: **CM**: Laboratoire de Cristallographie et Sciences des Matériaux (CRISMAT), 6 Blvd du Maréchal Juin 14050 CAEN CEDEX 4, France  
Ph.: +33.2.31.45.13.69; *E-mail address*: charles.maniere@ensicaen.fr

**Nomenclature** $\theta$  Porosity $\dot{\theta}$  Porosity rate ( $s^{-1}$ ) $\underline{\sigma}$  Stress tensor ( $N.m^{-2}$ ) $\sigma_{eq}$  Equivalent stress ( $N.m^{-2}$ ) $\underline{\dot{\epsilon}}$  Strain rate tensor ( $s^{-1}$ ) $\dot{\epsilon}_{eq}$  Equivalent strain rate ( $s^{-1}$ ) $\dot{\epsilon}_r$  Radial strain rate component ( $s^{-1}$ ) $\dot{\epsilon}_z$  Z strain rate component ( $s^{-1}$ ) $\dot{\epsilon}_{sintering}$  Free strain rate due to sintering ( $s^{-1}$ ) $\varphi$  Shear modulus $\psi$  Bulk modulus $P_l$  Sintering stress (Pa) $\mathbf{i}$  Identity tensor $\alpha$  Surface energy ( $J.m^{-2}$ ) $r$  Grain radius (m) $\dot{\epsilon}$  Trace of the strain rate tensor ( $s^{-1}$ ) $\eta$  Material viscosity (Pa.s) $K$  Bulk viscosity (Pa.s) $G$  Shear viscosity (Pa.s) $\nu_p$  Viscous Poisson's ratio $\eta_r$  Radial component of the viscosity (Pa.s) $\eta_z$  Z component of the viscosity (Pa.s) $\eta_0$  Viscosity pre-exponential factor (Pa.s) $\eta_{0r}$  Radial component of the viscosity pre-exponential factor (Pa.s) $\eta_{0z}$  Z component of the viscosity pre-exponential factor (Pa.s) $Q$  Viscosity activation energy ( $J.mol^{-1}$ ) $R$  Gas constant 8.314 ( $J.mol^{-1}.K^{-1}$ ) $T$  Temperature (K)**1. Introduction**

Ceramic additive manufacturing encompasses different methods capable of printing 3D ceramic objects by successive deposited layers. Among the existing approaches [1,2], we identify the following: “robocasting” based on the extrusion of a ceramic slurry, “binder jetting,” where a binder is selectively sprayed at the surface of a powder bed, and

stereolithography based on the UV polymerization of a ceramic/resin slurry [3]. The latter is the method that is considered further in this study. These approaches consist of printing a 3D green object that requires at least two additional thermal steps, a “debinding” step for removing the polymer phase, and a sintering step of the ceramic powdered green object. Depending on the method, these last two steps can be more or less difficult to implement. Ceramic robocasting typically has a rough resolution due to the large extrusion nozzle diameter (0.2–1 mm); however, it does offer a short processing time [4]. The main challenge of binder jetting is the low density of the printed green specimens, which makes full densification difficult [5]. Stereolithography is a slow process; however, it provides excellent resolution (down to approximately 25–100  $\mu\text{m}$  [6]), and a relatively high green density (45–60%), which facilitates full densification of the printed specimens [1]. This technique is also one of the oldest [7] and to date, one of the most reliable processes in terms of printing quality and repeatability.

Despite the previous cited advantages, the sintering of printed green specimens obtained by stereolithography remains a challenge. The first obstacle is the “debinding,” which requires burning the polymer phase while avoiding the formation of cracks and swelling phenomena [8,9]. In general, extremely slow debinding cycles at low temperatures with long dwell duration (approximately 10 hours) are required [10]. The other difficulty is the anisotropic nature of the sintering of the printed specimens, which tends to generate a distortion of the sintered object compared to the predicted theoretical isotropic shrinkage [11,12]. Anisotropy can result from different causes including the particle shape, structure and orientation, particle packing and porosity, and gravity [13–17]. As this anisotropy can have a strong influence on the sintering and homogeneity of the sintered compact, this phenomenon must be carefully examined. Therefore, the objective of this paper is investigate this phenomenon, which has been reported previously for other additive manufacturing techniques [18,19], in order to understand how successive layer deposition contributes to the anisotropy.

In this paper, an understanding of the origin of the anisotropy and how this phenomenon evolves during the sintering of printed materials is first developed. Based on the continuum theory of sintering [20], a model is developed to predict the sintering anisotropy during the sintering of the printed ceramics parts. This model must correctly address the sintering behavior of the printed specimen. It must also be easily convertible into finite element code and not strictly limited to an analytic treatment. One of the first obstacles encountered for the establishment of such a simulation study is a determination of the modeling parameters. Special care is given to the development of a method for identification of the anisotropic sintering behavior (based on dilatometry in two directions). Then, we provide a modeling tool readily useable for the prediction of stereolithography sintering.

## 2. Experiment and method

The printing experiments were made on the “Form 2” stereolithography model device from Formlabs. A silica resin from the same company called “ceramic resin” was employed. This resin is a mixture of acrylate based oligomer and silica particles that can be selectively photopolymerized by UV laser radiation. The debinding cycle recommended by the company for this resin was a 1 K/min heating ramp to 240 °C, then 8 h of holding, followed by a 1 K/min heating ramp to 300 °C, and 1 h of holding at this temperature. After the debinding, the recommended sintering cycle was to increase the temperature at 3 K/min to 1270 °C. We chose to perform the debinding (long process) and sintering separately, the latter being performed by dilatometry (Setaram TMA96). To prevent the debinded specimens from collapsing during the transfer into the dilatometer, a 3 K/min heating ramp to 900 °C was added to the debinding cycle to consolidate the specimens.

To study the sintering anisotropy through a dilatometry analysis, several 5 mm cubes were printed, debinded, and consolidated. The sintering cycle in the dilatometer was a 3 K/min heating ramp to 1270 °C followed by a 10 K/min cooling ramp to room temperature. The dilatometry was investigated in two configurations (Figure 1), one with the sintering

shrinkage measured on the printing building direction (perpendicular to the printing layers, “Z displacement”) and the other in the radial direction (parallel to the printing layers, “R displacement”). In this manner, from the two cubes with a 90° rotation, it was possible to quantify the shrinkage anisotropy. These data are analyzed in the modeling section.

To study the origin of the sintering anisotropy in this material, two additional experiments were performed, consisting of heating the materials to 1000 °C and 1130 °C with a 3 K/min heating ramp, followed by a 10 K/min cooling. The obtained specimens were polished and analyzed by SEM (JEOL 7200F) to observe the evolution of the porous skeleton and particle distribution.

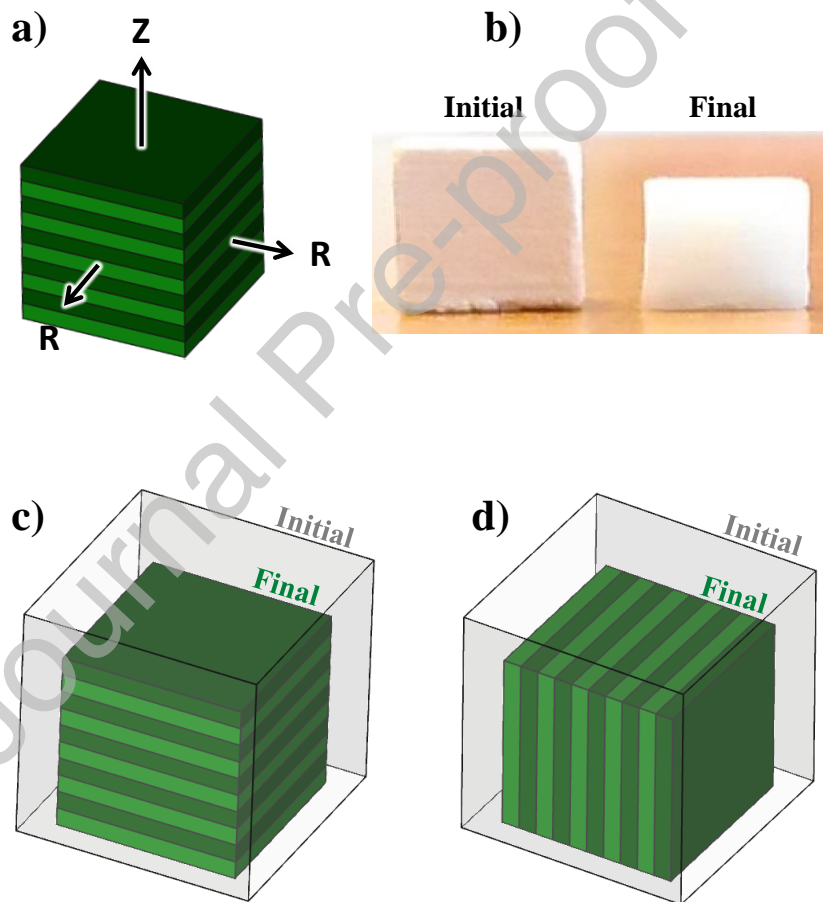


*Figure 1 a) Printed cube with representation of layer directions (R) and building direction (Z), b) printed and debinded cubes before and after sintering at 1270 °C, anisotropic shrinkage is clearly observable, c) Z-axis sintering dilatometry shrinkage measurement, d) R-axis sintering dilatometry shrinkage measurement; dilatometry shrinkage is always measured by top face displacement.*

### 3. Theory and calculations

The sintering model basis for this application must be implementable as a finite element code to allow predicting the influence of a highly complex shape, gravity, and friction on the sintering of different printed shapes. This model must also allow the simulation of the intrinsic anisotropic behavior of the printed specimens and must be reducible to analytic equations for easy identification of the model parameters. Considering this, Olevsky's model was chosen [20]. It describes the local sintering equations of a continuous compressible medium. This model contains theoretical relations for the sintering stress, compaction moduli, and thermal dependence of the viscosity of the material [21]. This study focuses on the analytic modeling and extraction of the anisotropy sintering parameters of the printed specimens.

#### 3.1. Sintering local equations

The local behavior of a continuous compressible medium is defined by the stress, and strain rate tensors general equation [20,22]:

$$\underline{\sigma} = \frac{\sigma_{eq}}{\dot{\epsilon}_{eq}} \left( \varphi \underline{\dot{\epsilon}} + \left( \psi - \frac{1}{3} \varphi \right) \dot{\epsilon} \mathbb{1} \right) + P_l \mathbb{1} \quad (1)$$

where  $\mathbb{1}$  is the identity tensor and  $P_l$  is the effective sintering stress (from sintering capillarity forces) defined by

$$P_l = \frac{3\alpha}{r} (1 - \theta)^2 \quad (2).$$

The equivalent strain rate  $\dot{\epsilon}_{eq}$  and stress  $\sigma_{eq}$  are related by the dense phase behavior. Pressureless sintering of non-nano powders is typically governed by a linear viscous behavior [23]. This is especially true for the case of silica sintering, which obeys the following viscous behavior:

$$\sigma_{eq} = 2\eta \dot{\epsilon}_{eq} \quad (3).$$

The temperature dependence of the material viscosity  $\eta$  has the general Arrhenius form [24]:

$$\eta = \eta_0 \exp\left(\frac{\psi}{RT}\right) \quad (4).$$

Equation (1) is then:

$$\underline{\sigma} = 2\eta \left( \varphi \underline{\dot{\epsilon}} + \left( \psi - \frac{1}{3} \varphi \right) \dot{\epsilon} \mathbb{1} \right) + P_l \mathbb{1} \quad (5).$$

The shear and bulk modulus ( $\varphi$  and  $\psi$ ) are functions of the porosity and depend on the porous skeleton morphology. These moduli can be theoretically approximated using Skorohod's equations [21]:

$$\varphi = (1 - \theta)^2 \quad (6)$$

$$\psi = \frac{2}{3} \frac{(1-\theta)^3}{\theta} \quad (7).$$

Alternatively, developing  $2\eta$  in (5), this expression can also be written using effective shear and bulk viscosities [20,25,26].

$$\underline{\sigma} = \left( K \dot{\epsilon} \mathbb{1} + 2G \left( \underline{\dot{\epsilon}} - \frac{1}{3} \dot{\epsilon} \mathbb{1} \right) \right) + P_l \mathbb{1} \quad (8)$$

with the expression of bulk viscosity  $K = 2\eta\psi$  and shear viscosity  $G = \eta\varphi$ . These effective viscosity terms gather the dense phase viscosity behavior,  $\eta$ , and porous behavior of the effective porous continuum described by the  $\varphi$  and  $\psi$  moduli. For linear sintering behavior such as free-sintering,  $K$  and  $G$  can be used directly as experimental functions that depend on the temperature and porosity.

The porosity  $\theta$  is determined by the local volume change through the mass conservation equation.

$$\frac{\dot{\theta}}{1-\theta} = \dot{\epsilon}_x + \dot{\epsilon}_y + \dot{\epsilon}_z \quad (9)$$

### 3.2. Isotropic pressureless sintering model

For pressureless isotropic viscous sintering, the analytic equations can be determined from the previous local equations if we consider the following simplifications:

$$\underline{\dot{\epsilon}} \equiv \begin{pmatrix} \dot{\epsilon}_r & 0 & 0 \\ 0 & \dot{\epsilon}_r & 0 \\ 0 & 0 & \dot{\epsilon}_r \end{pmatrix} \text{ Isotropic } \dot{\epsilon} = 3\dot{\epsilon}_r \quad (10).$$

Equation (5) is simplified and becomes

$$0 = 2\eta \left( \varphi \dot{\varepsilon}_r + \left( \psi - \frac{1}{3} \varphi \right) 3\dot{\varepsilon}_r \right) + P_l \quad (11).$$

Then, we obtain the relation

$$-P_l = 2\eta 3\dot{\varepsilon}_r \psi \quad (12).$$

Using the mass conservation equation (9), we obtain the isotropic sintering analytic equation

$$\dot{\theta} = \frac{-P_l(1-\theta)}{2\eta\psi} \quad (13).$$

### 3.3. Anisotropic pressureless sintering model

The anisotropic pressureless sintering equations for the printed specimens must consider a different behavior in the building direction (Z-axis in Figure 1) and the plane of the layers (R-axes in Figure 1). The effective porous behavior represented by the shear and bulk viscosity ( $G$  and  $K$ ) should be different in axes R and Z. In this study, the expressions of  $G$  and  $K$  consider (6), (7) moduli and the anisotropy is identified via the parameter  $\eta$  ( $\eta_z, \eta_r$ ). In this manner, both  $G$  and  $K$  functions are influenced by the anisotropic behavior ( $G_z, G_r, K_z, K_r$ ). This also allows correcting the porous behavior ( $\varphi$  and  $\psi$ ) in  $G$  and  $K$  by the identification of the effective viscosity.

The strain rate tensor is then simplified as

$$\underline{\dot{\varepsilon}} \equiv \begin{pmatrix} \dot{\varepsilon}_r & 0 & 0 \\ 0 & \dot{\varepsilon}_r & 0 \\ 0 & 0 & \dot{\varepsilon}_z \end{pmatrix} \text{ Anisotropic } \dot{\varepsilon} = 2\dot{\varepsilon}_r + \dot{\varepsilon}_z \quad (14).$$

The general form of equation (5) becomes

$$\underline{\sigma} = 2\eta \left( \varphi \underline{\dot{\varepsilon}} + \psi 2\dot{\varepsilon}_r \mathbb{1} - \frac{2\dot{\varepsilon}_r}{3} \varphi \mathbb{1} + \psi \dot{\varepsilon}_z \mathbb{1} - \frac{\dot{\varepsilon}_z}{3} \varphi \mathbb{1} \right) + P_l \mathbb{1} \quad (15).$$

In the plane of the printed layers (R-axes) and for pressureless sintering, we have

$$0 = 2\eta_r \left( \varphi \dot{\varepsilon}_r + \psi 2\dot{\varepsilon}_r - \frac{2\dot{\varepsilon}_r}{3} \varphi + \psi \dot{\varepsilon}_z - \frac{\dot{\varepsilon}_z}{3} \varphi \right) + P_l \quad (16).$$

Gathering the strain rates we obtain

$$\frac{-P_l}{2\eta_r} = \dot{\varepsilon}_r \left( 2\psi + \frac{\varphi}{3} \right) + \dot{\varepsilon}_z \left( \psi - \frac{\varphi}{3} \right) \quad (17).$$

Isolating the R strain rate component, we obtain

$$\dot{\epsilon}_r = \frac{\frac{-P_l}{2\eta_r} \dot{\epsilon}_z \left(\psi - \frac{\varphi}{3}\right)}{\left(2\psi + \frac{\varphi}{3}\right)} \quad (18).$$

In the building direction (Z-axis) and for pressureless sintering, we have

$$0 = 2\eta_z \left( \varphi \dot{\epsilon}_z + \psi 2\dot{\epsilon}_r - \frac{2\dot{\epsilon}_r}{3} \varphi + \psi \dot{\epsilon}_z - \frac{\dot{\epsilon}_z}{3} \varphi \right) + P_l \quad (19).$$

Gathering the strain rates we obtain

$$\frac{-P_l}{2\eta_z} = 2\dot{\epsilon}_r \left( \psi - \frac{\varphi}{3} \right) + \dot{\epsilon}_z \left( \psi + \frac{2\varphi}{3} \right) \quad (20).$$

Isolating the Z strain rate component, we obtain

$$\dot{\epsilon}_z = \frac{\frac{-P_l}{2\eta_z} - 2\dot{\epsilon}_r \left(\psi - \frac{\varphi}{3}\right)}{\left(\psi + \frac{2\varphi}{3}\right)} \quad (21).$$

Equations (18) and (21) are a system of two equations with two unknowns ( $\dot{\epsilon}_z$ ,  $\dot{\epsilon}_r$  output parameters of the model) and each equation has an expression of one strain rate component (R or Z) that depends on the other. However, to analytically solve this problem without circular variable dependence, we must combine these equations. Replacing  $\dot{\epsilon}_r$  in (21) by (18), we obtain the equation of  $\dot{\epsilon}_z$  that depends only on the known modeling parameters  $\eta_z$ ,  $\eta_r$  and the calculated variable depending on the porosity ( $\varphi$ ,  $\psi$ , and  $P_l$ ):

$$\dot{\epsilon}_z = \frac{\frac{-P_l}{2\eta_z} - \frac{-P_l}{\eta_r} \left(\psi - \frac{\varphi}{3}\right)}{\left(\psi + \frac{2\varphi}{3}\right) \left(2\psi + \frac{\varphi}{3}\right) \left(\psi + \frac{2\varphi}{3}\right)} \left(1 - \frac{2\left(\psi - \frac{\varphi}{3}\right)^2}{\left(2\psi + \frac{\varphi}{3}\right) \left(\psi + \frac{2\varphi}{3}\right)}\right) \quad (22).$$

#### 3.4. Identification equations of the viscous parameters

Based on the experimental data obtained by dilatometry in the R and Z directions, we can determine  $\theta$ ,  $\varphi$ ,  $\psi$ ,  $\dot{\epsilon}_r$ , and  $\dot{\epsilon}_z$ . Then, using equations (18) and (21), it is possible to obtain experimentally the value of the anisotropic viscous behavior. From this, we can determine the following equations that isolate the unknown viscosity terms.

$$\eta_r = \frac{-P_l}{2 \left( \dot{\epsilon}_r + \dot{\epsilon}_z \frac{\left(\psi - \frac{\varphi}{3}\right)}{\left(2\psi + \frac{\varphi}{3}\right)} \right) \left(2\psi + \frac{\varphi}{3}\right)} \quad (23)$$

$$\eta_z = \frac{-r_l}{2 \left( \dot{\varepsilon}_z + 2\dot{\varepsilon}_r \left( \frac{\psi - \frac{\varphi}{3}}{2\psi + \frac{\varphi}{3}} \right) \right) \left( \psi + \frac{2\varphi}{3} \right)} \quad (24)$$

If we develop the expression of the Laplace sintering stress  $P_l$ , there is one additional unknown, the surface energy  $\alpha$ . However, in Equations (18) and (21), this unknown appears in the form of a ratio of the sintering stress and viscosity. Then, developing the expression of the sintering stress and viscosity, we can circumvent this problem using the direct identification of the ratio of the viscosity pre-exponential constant and surface energy [27,28].

The following regression equations are obtained.

$$Y_r = \ln \left( \frac{-3(1-\theta)^2}{2r \left( \dot{\varepsilon}_r + \dot{\varepsilon}_z \left( \frac{\psi - \frac{\varphi}{3}}{2\psi + \frac{\varphi}{3}} \right) \right) \left( 2\psi + \frac{\varphi}{3} \right)} \right) = \ln \left( \frac{\eta_{0r}}{\alpha} \right) + \frac{Q}{RT} \quad (25)$$

$$Y_z = \ln \left( \frac{-3(1-\theta)^2}{2r \left( \dot{\varepsilon}_z + 2\dot{\varepsilon}_r \left( \frac{\psi - \frac{\varphi}{3}}{2\psi + \frac{\varphi}{3}} \right) \right) \left( \psi + \frac{2\varphi}{3} \right)} \right) = \ln \left( \frac{\eta_{0z}}{\alpha} \right) + \frac{Q}{RT} \quad (26)$$

#### 4. Results and discussions

In this section, the experimental results of the sintering experiments and the analysis of the microstructures are presented. Based on these data, the sintering model parameters are identified and the resulting model is compared to the experimental results.

##### 4.1. Powder morphology

The SEM images of the silica powder obtained after 700 °C calcination and after sintering at 1000 °C are reported in Figure 2. The silica powder obtained after burning the polymer phase in air at 700 °C demonstrated a large particle-size distribution. The sample sintered to 1000 °C (with no dwell time) confirmed this extremely large grain distribution. There was a population of three particles sizes. The first population was characterized by small grains with a diameter less than 1  $\mu\text{m}$ , a second population with spherical particles between 2  $\mu\text{m}$  and 10  $\mu\text{m}$ , and a third population with large grains, with a complex shape and a size greater than

20  $\mu\text{m}$ . The powder average particle diameter was 5.44  $\mu\text{m}$ . It is likely that the Formlabs company chose this grain distribution to obtain an optimal packing density of the particles before sintering. The SEM image of the sintered specimen at 1000  $^{\circ}\text{C}$  indicates a microstructure with extremely high grain compactness despite the fact that the shrinkage value is rather low (this is discussed later). It must be emphasised that this microstructure image was captured in the center of a printed layer, where the porosity was minimal. We observe later that the amount of porosity increases between the printed layers, for an overall green specimen relative density close to 50%.

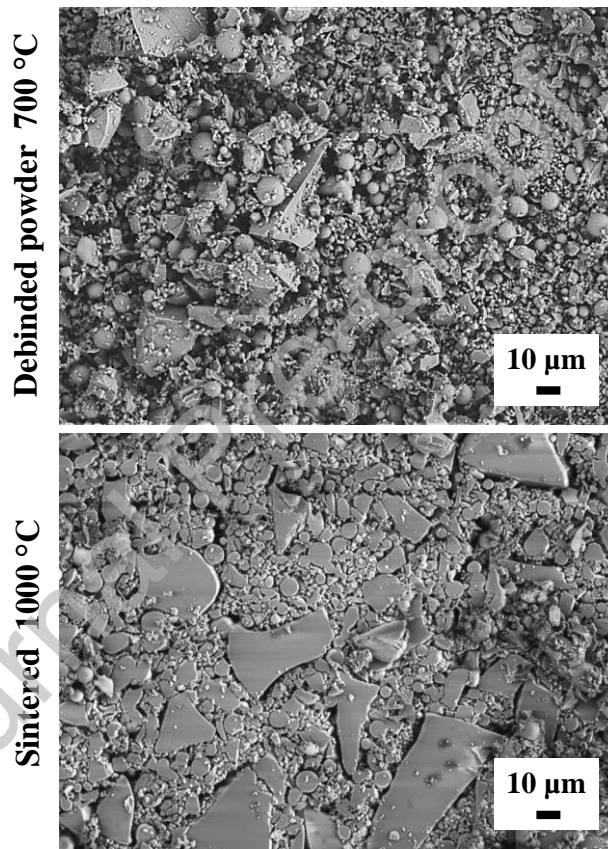


*Figure 2 SEM images of: (upper) the powder obtained after 700  $^{\circ}\text{C}$  calcination of ceramic resin in air and (lower) polished surface of printed specimen sintered at 3 K/min up to 1000  $^{\circ}\text{C}$ .*

## 4.2. Sintering dilatometry results

The results of the dilatometry experiments in the R and Z configurations are reported in Figure 3. The displacement and strain rate curves clearly indicate the anisotropic behavior of the printed specimens during the sintering. In the building direction (Z-axis), the sintering shrinkage and strain rate are greater. However, the shape and temperature responses of these two curves are similar. The strain rate peaks are not shifted indicating a similar viscosity temperature dependence, yet a significant difference in magnitude is clearly observed (anisotropy). The displacement ratio Z/R presents a curve that appears to stabilize as the sintering process is progressing. This indicates an extremely strong anisotropic response at the beginning of the sintering and a behavior that tends to become isotropic at the end of the sintering.

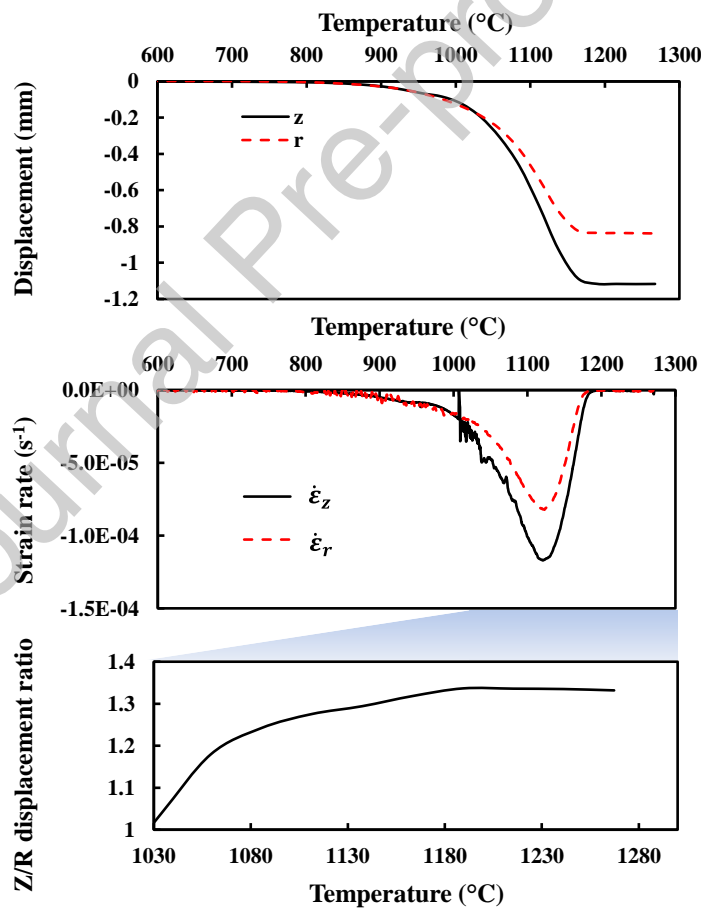


Figure 3 a) Sintering displacement curves in R and Z directions, b) calculated corresponding strain rates and, c) evolution of R and Z displacements ratio.

Using the dilatometry data in the R and Z direction, it is possible to determine the geometrical relative density curve reported in Figure 4. The printed specimen has an initial relative density

of 0.5; it begins sintering at 1000 °C and the process terminates at approximately 1170 °C.

The shape of this densification curve indicates a slow sintering behavior in the beginning (likely owing to the complex distribution of the powder) and an abrupt ending stage at approximately 0.95 relative density. The densification appears to drastically decelerate at this relative density despite the increasing temperature. This could be explained by the presence of large pores, which are difficult to remove.

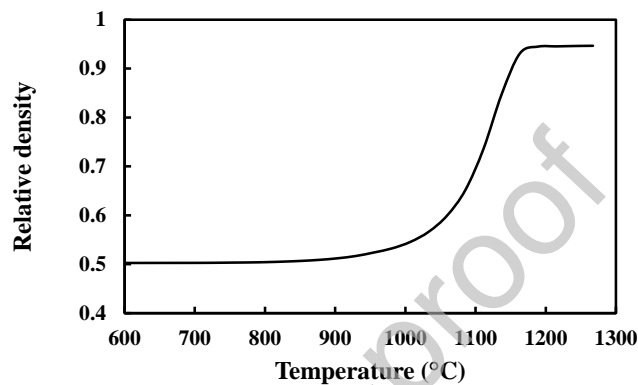


Figure 4 Relative density curve of printed silica specimen sintering.

#### 4.3. Microstructure of the printed and sintered specimen, origin of the anisotropy

The microstructures along the Z-axis of the sintered specimens at 1270 °C and of the two interrupted cycle samples at 1000 °C and 1130 °C are reported in Figure 5. The microstructures demonstrate large porous areas that appear to be located between the printed layers. These porous areas appear as large cracks at 1130 °C. However, these cracks are likely lines of porous interlayer gradient as large cracks do not sinter and do not create anisotropy. They are likely due to material losses in these fragile areas during the cutting/polishing process. These highly porous interlayer lines appear to exhibit a pore coalescence phenomenon at high temperatures (1270 °C), which leaves large pores lines at the end of the sintering. Around these large pores, the presence of microcracks is also visible. It appears that the printing process generates an intrinsic area between the layers where the UV polymerization (or the layer transition) implies a nonuniform particle distribution or the presence of cracks after the debinding. The simulation of the UV laser exposure in [29]

indicates a non-ideal interlayer exposure, which seems to justify this hypothesis. Moreover, the “bottom-up” stereolithography mode uses a laser that crosses a transparent window and consolidates the resin, which can have a degree of adhesion with the transparent window and poor adhesion with the previously printed layer. This also could explain the higher interlayer porosity in the green specimens.

Despite the presence of the 5 % of final specimen porosity originating from the interlayer printing process, the overall microstructure (at 1270 °C) is well sintered, which explains the translucent aspect of the sintered specimen in Figure 1b.

The origin of the sintering anisotropy then, is a consequence of an architected porous microstructure characterized by an important local porous structure in the interlayer area. This configuration generates less resistance to deformation in the building direction (Z-axis) owing to the preferential elimination of the pores between the layers. On the opposite, in R-axis, the specimen shrinkage is limited by the middle layer area which has a lower porosity level and a higher resistance to shrinkage. The shear and bulk viscosity  $G_z$ ,  $G_r$  and  $K_z$ ,  $K_r$  reflects the fact that the effective viscosity is lower in building layer direction (Z-axis). The fact that the anisotropy is due to a porosity gradient explains why the shrinkage anisotropy behavior tends to an isotropic behavior at the end of the sintering. The anisotropic porous distribution slowly vanishes with the elimination of the porosity. If the origin of the anisotropy was because of the shape of the particles, this anisotropy would be preserved owing to the oriented microstructure at the end of the sintering stage. The presence of large pores at the end of the sintering also explains why the sintering abruptly terminates at the end. When the well-compacted layer phase is fully dense, the large pores between the layers require an extended period to be removed by the weak Laplace surface tension they develop.

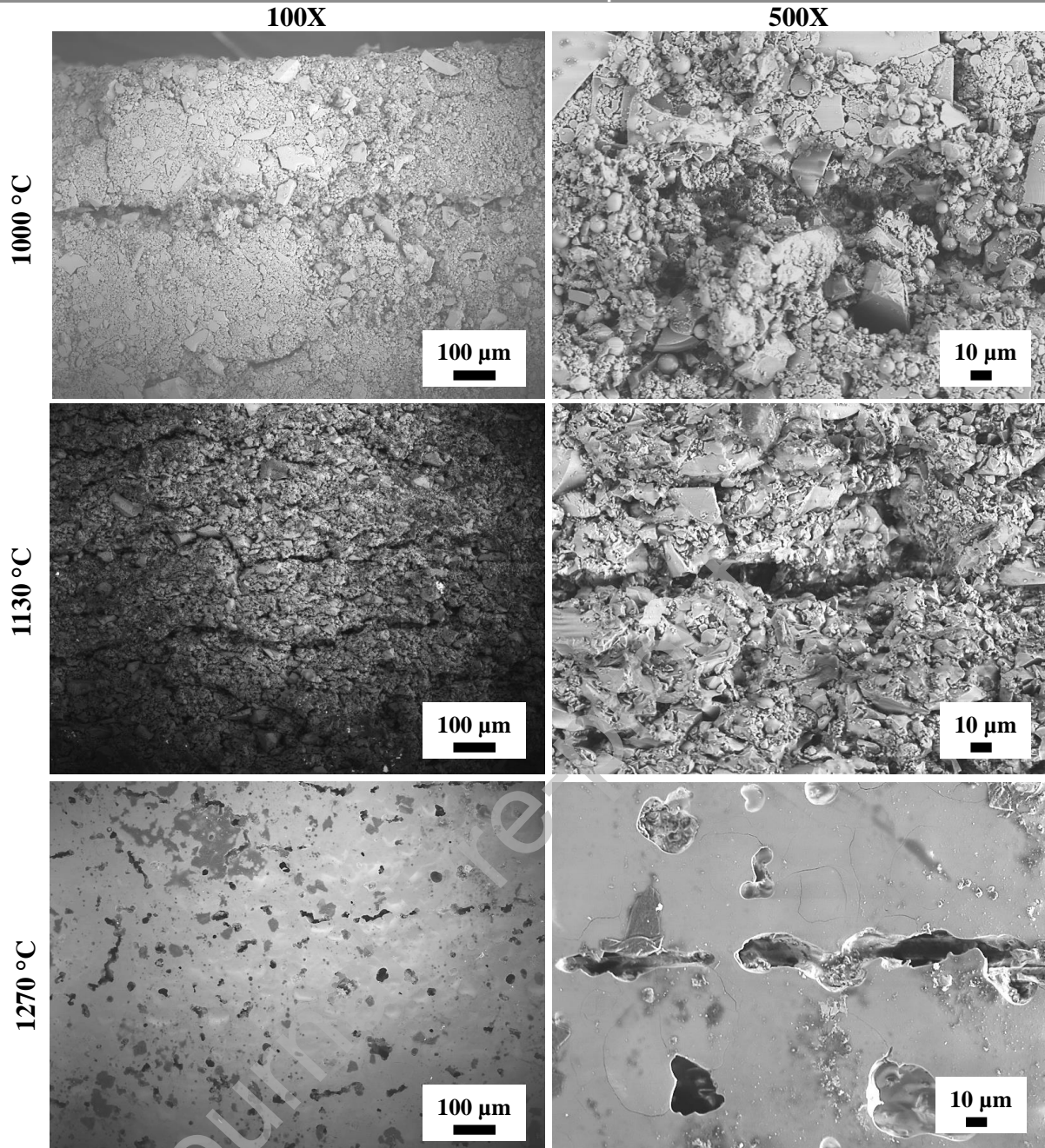


Figure 5 SEM images of cubes sintered at 3 K/min to temperatures 1000 °C, 1130 °C, and 1270 °C; for all images, building direction (Z-axis) is from bottom to top; right images at 500X are zoom of interlayer areas.

## 4.4. Identification of the anisotropic sintering parameters

Previous dilatometry and microstructures suggest an anisotropic behavior originating from an architected pore distribution. From a mechanical point of view, this implies an equivalent anisotropic viscous behavior, which disappears as the sintering progresses and a similar temperature dependence of the apparent viscosity (same activation energy). To simulate the abrupt sintering plateau (ending stage) due to the large porosity, we modified the expression of the bulk modulus (27) using a critical porosity (0.05), which makes the modulus tend to infinity for a densification of 95% rather than 100%. This is equivalent to considering the theoretical moduli (7) applied to the phase surrounding the large pores instead of the entire microstructure, which has a multiscale porosity. As indicated in the models in Figure 6, the model with critical porosity best describes the plateau of the densification curve at the end of the sintering.

$$\psi = \frac{2}{3} \frac{(1-\theta)^3}{(\theta-0.05)} \quad (27).$$

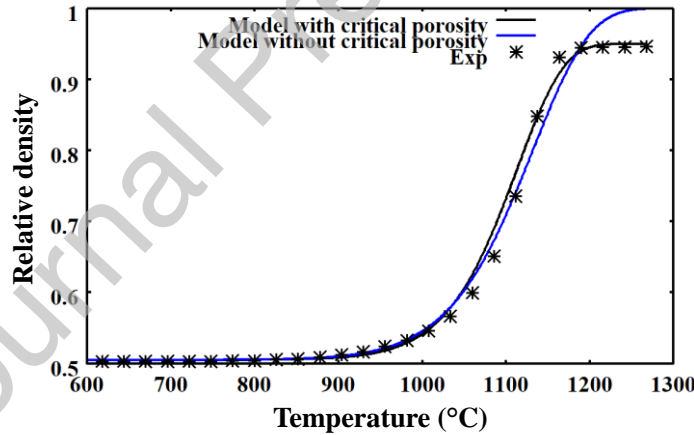


Figure 6 Sintering models with and without critical porosity in bulk modulus expression.

Using the dilatometry data and regression equations (25) and (26), the anisotropy assumptions previously formulated were tested. The graphs of these equations are displayed in Figure 7. Both curves indicate a unique activation energy close to  $290 \text{ kJ.mol}^{-1}$  and a value of pre-exponential ratio corresponding to a lower apparent viscosity in the building direction (Z-axis). This is in accordance with the higher sintering shrinkage in this direction.

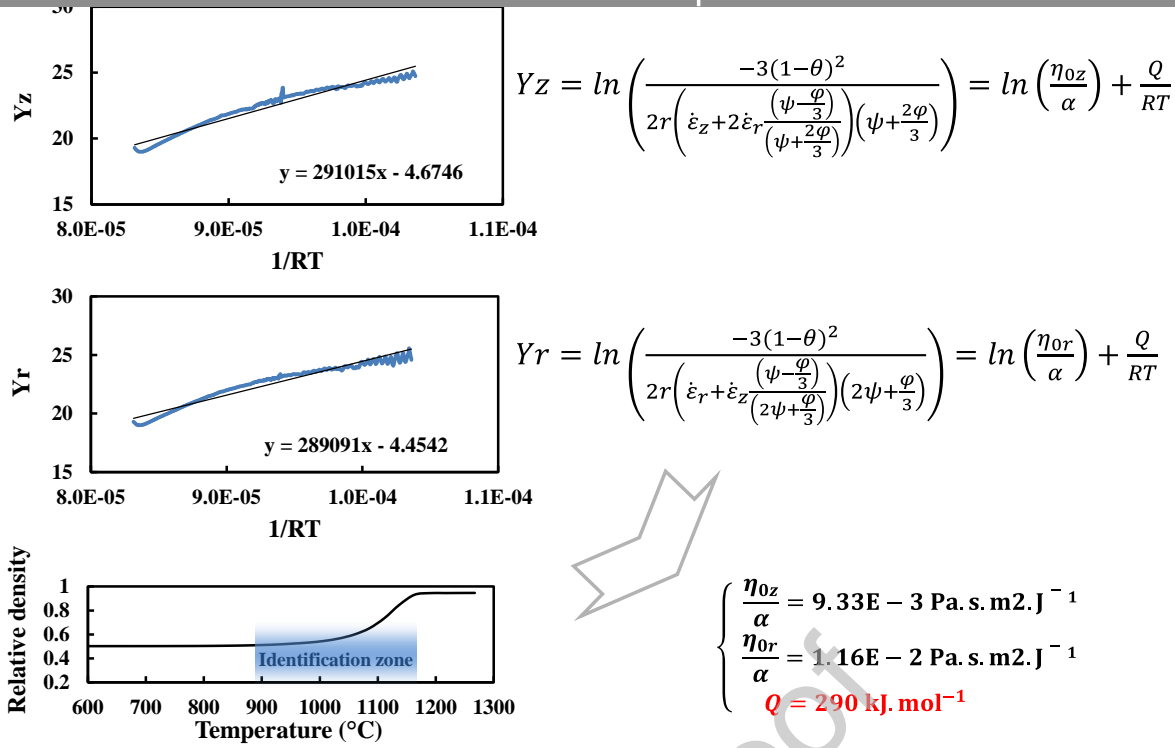


Figure 7 Regression analysis using R and Z-axis dilatometry data for extraction of viscosity parameters.

However, the fitting of the curve is not perfectly linear, indicating that a pre-exponential ratio could evolve. We have previously discussed the phenomena of attenuation of the anisotropy as the porosity is removed from the material, and the relationship between the pore architecture and anisotropy. This phenomenon cannot be considered if the pre-exponential ratio responsible for the anisotropy in the model is constant. Therefore, the pre-exponential factor could have a porous dependence to predict the attenuation of the anisotropy. Equations (25) and (26) were rearranged in Equations (28) and (29) to model the porous evolution of the pre-exponential factor. The activation energy was fixed to the value of  $290 \text{ kJ.mol}^{-1}$  indicated by both previous equations (Figure 7).

$$\frac{-3(1-\theta)^2}{2r \left( \dot{\epsilon}_r + \dot{\epsilon}_z \frac{\left(\psi - \frac{\varphi}{3}\right)}{\left(2\psi + \frac{\varphi}{3}\right)} \right) \exp\left(\frac{Q}{RT}\right)} = \frac{\eta_{0r}(\theta)}{\alpha} \quad (28)$$

$$\frac{-3(1-\theta)^2}{2r \left( \dot{\epsilon}_z + 2\dot{\epsilon}_r \frac{\left(\psi - \frac{\varphi}{3}\right)}{\left(\psi + \frac{2\varphi}{3}\right)} \right) \exp\left(\frac{Q}{RT}\right)} = \frac{\eta_{0z}(\theta)}{\alpha} \quad (29)$$

The pre-exponential factors  $\frac{\eta_{or}(\theta)}{\alpha}$  and  $\frac{\eta_{oz}(\theta)}{\alpha}$  obtained using (28) and (29) are presented in Figure 8. The attenuation of the anisotropy with the sintering clearly appears here. The pre-exponential factor for values of porosity between 0.5 and 0.2 indicates a clearly reduced viscosity in the building direction (Z-axis), and a high anisotropy at the beginning of the sintering process. For reduced porosity, both curves are virtually identical indicating a quasi-isotropic behavior in accordance with the porous origin of the anisotropy phenomenon.

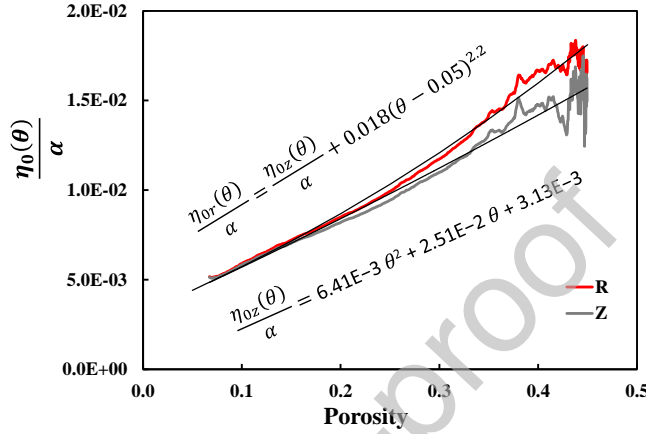


Figure 8 Pre-exponential factor porous dependence and their fitting equations.

#### 4.5. Analytic modeling of the printed specimen sintering

Using the previously determined sintering parameters  $Q$ ,  $\frac{\eta_{or}(\theta)}{\alpha}$ , and  $\frac{\eta_{oz}(\theta)}{\alpha}$ , which provide the functions  $\frac{\eta_r(T,\theta)}{\alpha}$  and  $\frac{\eta_z(T,\theta)}{\alpha}$ , the analytic modeling of the anisotropic sintering of the printed specimen is investigated. This model solves, in the following order, Equations (2), (6), (7), (22), (18), and (9). Introducing the sintering stress equation  $P_l$  (2) and the shear and bulk moduli  $\varphi$ ,  $\psi$  (6) (7) in Equation (22), it is possible to determine  $\dot{\epsilon}_z$ , then, introducing  $\dot{\epsilon}_z$  in Equation (18),  $\dot{\epsilon}_r$  can be obtained. Knowing  $\dot{\epsilon}_z$  and  $\dot{\epsilon}_r$ , the porosity can be calculated using the mass conservation equation (9). The displacements in R and Z are calculated by integration of the corresponding strain rates and using the log form of the true strain [30]. These calculations were performed on Octave-Forge software using the initial value  $\theta = 0.495$ . The results of the analytic modeling are reported in Figure 9. These results confirm that

the proposed identification method provides parameter values that can reproduce the experimental results with a reasonable error (less than 5%).

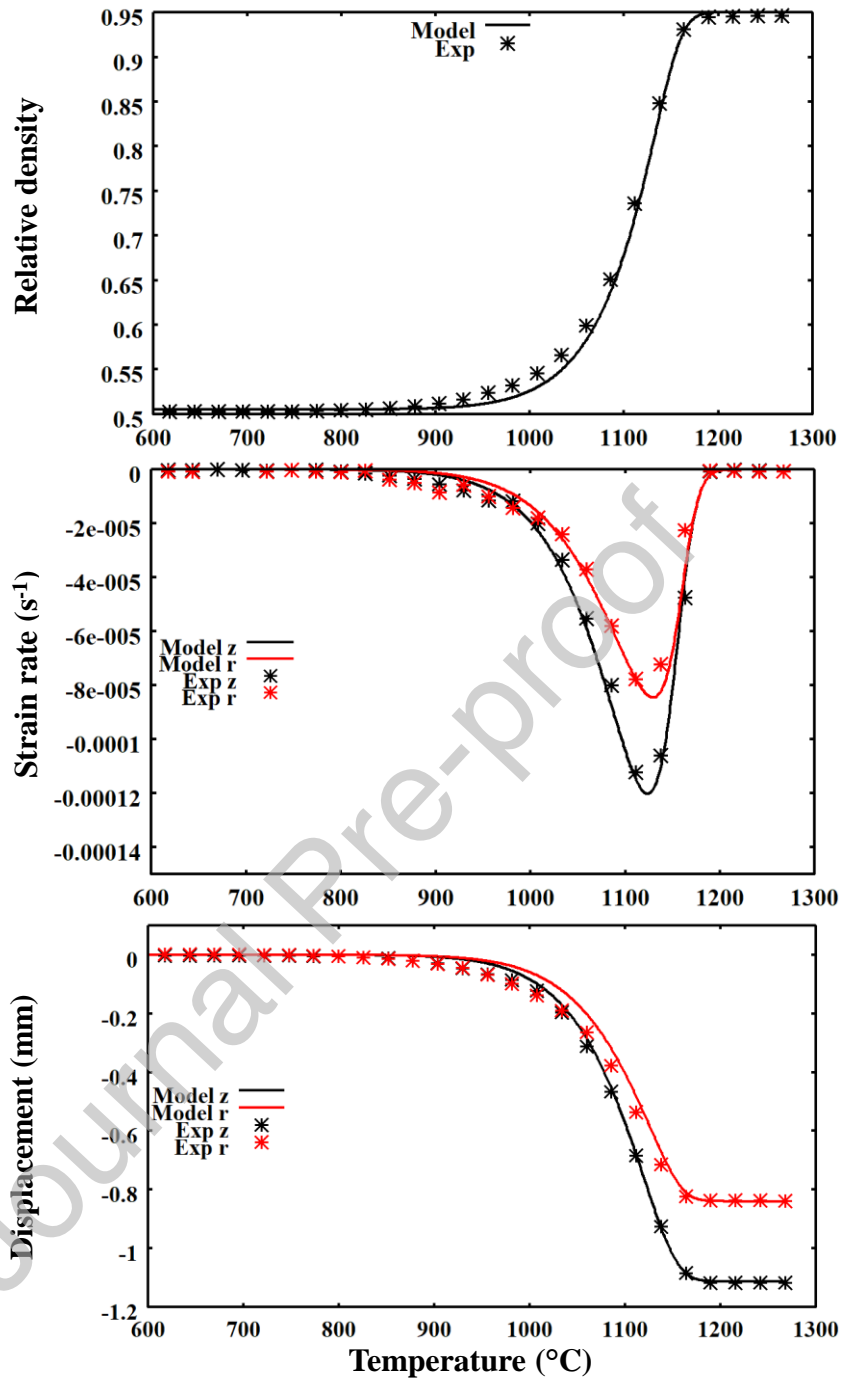


Figure 9 Modeled analytical curves of anisotropic sintering versus experimental data.

## 5. Conclusion

The sintering behavior of stereolithography printed silica specimens was studied through dilatometry and modeling approaches. The dilatometry experiments recorded in two printing axes reveal the highly anisotropic nature of the sintering of the printed specimens. The SEM microstructure of the specimens captured at different temperatures explains the origin of this anisotropy, which is related to the non-ideal porosity distribution between the different printing layers. In this area, the particle packing is less dense generating considerable porosity and a number of cracks. This architected porous microstructure has three main consequences: (i) a higher sintering shrinkage in the building direction, (ii) the anisotropic behavior is slowly attenuated with the removal of the porosity to tend to an isotropic behavior at the end of the sintering, and (iii) the high interlayer porosity generates a pore coalescence phenomenon, which creates lines of large pores difficult to remove by pressureless sintering. Despite this anisotropic sintering nature, the studied ceramic resin provides printed specimens with a high pre-sintering compaction, 50%, which allows a sintering up to a high final densification (less than 5% of post-sintering porosity). Furthermore, our experiments on small specimens indicate this anisotropic sintering behavior is highly reproducible. Based on the continuum theory of sintering, we developed an analytic formulation of the anisotropic sintering. These equations were used for the identification of the sintering parameters (from dilatometry data) and for the modeling of the sintering. This model predicts the anisotropic sintering behavior of a continuum. The complex mesoscale sintering phenomena such as cracks, the pore coalescence/gradients, and the influence of the multi-modal particle distribution on the sintering mechanism require more advanced *in situ* studies of the sintering. The sintering parameters identified by the present method can be used in a finite element code to predict the sintering distortions of more advanced complex shapes and to conduct optimization studies on real size printed parts.

In the literature, there are numerous free sintering models that can simulate free sintering. We chose Olevsky's model for our study. In this appendix, we discuss how this model can be compared to the others. We demonstrated in Section 3.1. that Olevsky's model represented by Eq. (5) can be written in the form of Eq. (8) using the shear and bulk viscosity ( $G$  and  $K$ ), as in the Riedel *et al.* model [26]. Another form of a free sintering model using viscous Poisson's ratio  $\nu_p$  is used by numerous other authors [31] and has the form below.

$$\underline{\dot{\epsilon}} = \frac{1}{2\eta} \left( (1 + \nu_p) \underline{\sigma} - \nu_p I_1 \underline{\mathbb{I}} \right) + \dot{\epsilon}_{sintering} \underline{\mathbb{I}} \quad (30)$$

This model can be written in the following form:

$$\underline{\dot{\epsilon}} = \frac{1}{2\eta} \left( (1 + \nu_p) \underline{S} + \left( \frac{1-2\nu_p}{3} \right) I_1 \underline{\mathbb{I}} \right) + \dot{\epsilon}_{sintering} \underline{\mathbb{I}} \quad (31).$$

This can then be easily compared to the Olevsky's model form below [20,30,32].

$$\underline{\dot{\epsilon}} = \frac{1}{2\eta} \left( \frac{S}{\varphi} + \frac{1}{9\psi} I_1 \underline{\mathbb{I}} \right) - \frac{P_l}{6\eta\psi} \underline{\mathbb{I}} \quad (32)$$

Comparing (31) and (32), it is clear that  $\nu_p$  can be assimilated to functions of the  $\varphi$  and  $\psi$  moduli of the Olevsky's model. Similarly, this indicates that  $\dot{\epsilon}_{sintering}$  is detailed in Olevsky's model by a function,  $-P_l/(6\eta\psi)$ , using the Laplace sintering stress, bulk modulus, and viscosity.

In summary, the previously cited free sintering models are similar, yet defined with different sintering parameters, which are typically identified experimentally.

### Acknowledgements

The help and support of Christelle Bilot and Jérôme Lecourt is gratefully acknowledged.

- [1] T. Chartier, A. Badev, Rapid Prototyping of Ceramics, in: *Handb. Adv. Ceram.*, Elsevier, 2013: pp. 489–524. doi:10.1016/B978-0-12-385469-8.00028-9.
- [2] J. Deckers, J. Vleugels, J.P. Kruth, Additive Manufacturing of Ceramics: A Review, *J. Ceram. Sci. Technol.* 5 (2014) 245–260. doi:10.4416/JCST2014-00032.
- [3] P.J. Bártolo, *Stereolithography*, Springer US, Boston, MA, 2011. doi:10.1007/978-0-387-92904-0.
- [4] E. Feilden, E.G.-T. Blanca, F. Giuliani, E. Saiz, L. Vandeperre, Robocasting of structural ceramic parts with hydrogel inks, *J. Eur. Ceram. Soc.* 36 (2016) 2525–2533. doi:10.1016/j.jeurceramsoc.2016.03.001.
- [5] J.A. Gonzalez, J. Mireles, Y. Lin, R.B. Wicker, Characterization of ceramic components fabricated using binder jetting additive manufacturing technology, *Ceram. Int.* 42 (2016) 10559–10564. doi:10.1016/j.ceramint.2016.03.079.
- [6] T. Chartier, C. Duterte, N. Delhote, D. Baillargeat, S. Verdeyme, C. Delage, C. Chaput, Fabrication of Millimeter Wave Components Via Ceramic Stereo- and Microstereolithography Processes, *J. Am. Ceram. Soc.* 91 (2008) 2469–2474. doi:10.1111/j.1551-2916.2008.02482.x.
- [7] C.W. Hull, Method for production of three-dimensional objects by stereolithography, US5762856A, 1998. www.google.com/patents/US4929402.
- [8] H. Li, L. Song, J. Sun, J. Ma, Z. Shen, Dental ceramic prostheses by stereolithography-based additive manufacturing: potentials and challenges, *Adv. Appl. Ceram.* 118 (2019) 30–36. doi:10.1080/17436753.2018.1447834.
- [9] C.-J. Bae, J.W. Halloran, Influence of Residual Monomer on Cracking in Ceramics Fabricated by Stereolithography, *Int. J. Appl. Ceram. Technol.* 8 (2011) 1289–1295. doi:10.1111/j.1744-7402.2010.02578.x.
- [10] H. Wu, Y. Cheng, W. Liu, R. He, M. Zhou, S. Wu, X. Song, Y. Chen, Effect of the particle size and the debinding process on the density of alumina ceramics fabricated by 3D printing based on stereolithography, *Ceram. Int.* 42 (2016) 17290–17294. doi:10.1016/j.ceramint.2016.08.024.
- [11] M. Lasgorceix, E. Champion, T. Chartier, Shaping by microstereolithography and sintering of macro-micro-porous silicon substituted hydroxyapatite, *J. Eur. Ceram. Soc.* 36 (2016) 1091–1101. doi:10.1016/j.jeurceramsoc.2015.11.020.
- [12] D.C. Aduba, K.C. Feller, C.B. Williams, An investigation of build orientation on shrinkage in sintered bioceramic parts fabricated by vat photopolymerization, *Proc. 28th Annu. Int. Solid Free. Fabr. Symp.* (2017) 2326–2340.
- [13] A. Zavaliangos, J.M. Missiaen, D. Bouvard, Anisotropy in shrinkage during sintering, *Sci. Sinter.* 38 (2006) 13–25. doi:10.2298/SOS0601013Z.
- [14] I.O. Ozer, E. Suvaci, B. Karademir, J.M. Missiaen, C.P. Carry, D. Bouvard, Anisotropic Sintering Shrinkage in Alumina Ceramics Containing Oriented Platelets, *J. Am. Ceram. Soc.* 89 (2006) 1972–1976. doi:10.1111/j.1551-2916.2006.01039.x.
- [15] O. Lame, D. Bouvard, H. Wiedemann, Anisotropic shrinkage and gravity induced creep during sintering of steel powder compacts, *Powder Metall.* 45 (2002) 181–185. doi:10.1179/pom.2002.45.2.181.
- [16] E.A. Olevsky \*, B. Kushnarev, A. Maximenko, V. Tikare, M. Braginsky, Modelling of

- anisotropic sintering in crystalline ceramics, *Philos. Mag.* 85 (2005) 2123–2146. doi:10.1080/14786430412331331989.
- [17] H. Shang, A. Mohanram, E. Olevsky, R.K. Bordia, Evolution of anisotropy in hierarchical porous ceramics during sinter-forging, *J. Eur. Ceram. Soc.* 36 (2016) 2937–2945. doi:10.1016/j.jeurceramsoc.2015.12.042.
- [18] C.S. Lee, S.G. Kim, H.J. Kim, S.H. Ahn, Measurement of anisotropic compressive strength of rapid prototyping parts, *J. Mater. Process. Technol.* 187–188 (2007) 627–630. doi:10.1016/j.jmatprotec.2006.11.095.
- [19] W. Cooke, R. Anne Tomlinson, R. Burguete, D. Johns, G. Vanard, Anisotropy, homogeneity and ageing in an SLS polymer, *Rapid Prototyp. J.* 17 (2011) 269–279. doi:10.1108/13552541111138397.
- [20] E.A. Olevsky, Theory of sintering: from discrete to continuum, *Mater. Sci. Eng. R Reports.* 23 (1998) 41–100. doi:10.1016/S0927-796X(98)00009-6.
- [21] V.V. Skorohod, Rheological basis of the theory of sintering, *Nauk. Dumka, Kiev.* (1972).
- [22] R.K. Bordia, S.-J.L. Kang, E.A. Olevsky, Current understanding and future research directions at the onset of the next century of sintering science and technology, *J. Am. Ceram. Soc.* 100 (2017) 2314–2352. doi:10.1111/jace.14919.
- [23] M.N. Rahaman, *Sintering of Ceramics*, CRC Press, 2007.
- [24] R.M. German, *Sintering Theory and Practice*, Wiley, Wiley, 1996. <http://www.wiley.com/WileyCDA/WileyTitle/productCd-047105786X.html>.
- [25] V. V. Skorokhod, M.B. Shtern, I.F. Martynova, Theory of nonlinearly viscous and plastic behavior of porous materials, *Sov. Powder Metall. Met. Ceram.* 26 (1987) 621–626. doi:10.1007/BF00810620.
- [26] H. Riedel, H. Zipse, J. Svoboda, Equilibrium pore surfaces, sintering stresses and constitutive equations for the intermediate and late stages of sintering—II. Diffusional densification and creep, *Acta Metall. Mater.* 42 (1994) 445–452. doi:10.1016/0956-7151(94)90499-5.
- [27] C. Manière, S. Chan, G. Lee, J. McKittrick, E.A. Olevsky, Sintering dilatometry based grain growth assessment, *Results Phys.* 10 (2018) 91–93. doi:10.1016/j.rinp.2018.05.014.
- [28] C. Manière, E. Saccardo, G. Lee, J. McKittrick, A. Molinari, E.A. Olevsky, Swelling negation during sintering of sterling silver: An experimental and theoretical approach, *Results Phys.* 11 (2018) 79–84. doi:10.1016/j.rinp.2018.08.035.
- [29] J. Tarabeux, V. Pateloup, P. Michaud, T. Chartier, Development of a numerical simulation model for predicting the curing of ceramic systems in the stereolithography process, *J. Eur. Ceram. Soc.* 38 (2018) 4089–4098. doi:10.1016/j.jeurceramsoc.2018.03.052.
- [30] C. Manière, E.A. Olevsky, Porosity dependence of powder compaction constitutive parameters: Determination based on spark plasma sintering tests, *Scr. Mater.* 141 (2017) 62–66. doi:10.1016/j.scriptamat.2017.07.026.
- [31] R. Bordia, R. Zuo, O. Guillon, S. Salamone, J. Rodel, Anisotropic constitutive laws for sintering bodies, *Acta Mater.* 54 (2006) 111–118. doi:10.1016/j.actamat.2005.08.025.
- [32] T.M. Tesfaye, PhD, Modeling Macroscopic Shape Distortions during Sintering of Multi-layers, Technical University of Denmark, 2014. <https://core.ac.uk/display/43245876>.

# CERAMIC STEREOLITHOGRAPHY

